Influence of solution parameters for the fast growth of ZnO nanostructures by laser-induced chemical liquid deposition

Christian Fauteux[1*], My Ali El Khakani[2], Joseph Pegna[1], Daniel Therriault[1]

[1]Center for applied research on polymers and composites (CREPEC), Department of Mechanical Engineering, École Polytechnique de Montréal, 2900 boul. Édouard-Montpetit, Montréal (QC), Canada

[2]Institut National de la Recherche Scientifique, INRS-Énergie, Matériaux et Télécommunications, 1650 boul. Lionel-Boulet, Varennes (QC), Canada

*Corresponding author. E-mail: christian.fauteux@polymtl.ca, postal address: C.P. 6079, succ. Centre-ville, Montréal (QC), Canada H3C 3A7, tel: 514-340-4711-7448, fax: 514-340-4176.

Abstract

ZnO nanorods, nanoneedles, nanoparticles and nanoballs were synthesized on fused quartz substrates upon irradiation of a droplet of methanolic zinc acetate dihydrate solution by an infrared continuous wave CO_2 laser for a few seconds. The addition of monoethanolamine and water to the solution improved the alignment of the nanorods and had a significant effect on the volume and morphology of the deposits. An increase of the zinc acetate concentration was found to lead to an increase of the thickness and area covered by the initial ZnO seed layer on which the nanostructures grew. By investigating the crystal structure of the deposits using x-ray and electron diffraction, we were able to show that the nanorods grow along the *c* axis with a high crystalline quality. Raman and photoluminescence spectroscopy confirmed the high-quality

of the grown ZnO nanostructures. As a matter of fact, their photoluminescence spectra are dominated by an intense UV emission around 390 nm.

PACS:81.05.Je; 81.10.Dn; 81.16.Mk; 82.80.Gk; 78.55.Hx

1. Introduction

Few materials exhibit as many valuable physical properties as zinc oxide. Being a UV-absorbing transparent semiconductor with a large exciton binding energy of 60 meV, zinc oxide is definitely a highly promising material for novel optoelectronic applications in the near future [1]. Recent advances in solid-vapour phase sublimation synthesis have shown that zinc oxide can be synthesized in a wide variety of nanostructured shapes which present tuneable properties [2]. Although nanostructured ZnO has now been produced using a variety of methods (such as metal-organic chemical vapour deposition [3], thermal evaporation [4] and oxidation [5], pulsed laser deposition [6] and template-based growth [7]), wet chemistry methods are becoming increasingly popular. These include hydrothermal processing [8], solution chemistry [9], seed layer-assisted aqueous growth [10] and sol-gel synthesis [11]. These milder techniques offer various advantages as they generally use non-toxic reagents, allow extensive control over nanostructure alignment and morphology, and could be relatively easily scaled-up to meet the industrial needs. Nevertheless, their main drawback is the long processing times. For instance, the controlled growth of arrays of ZnO nanotubes [12] or nanorods [13] can easily take days due to the use of diluted precursor solution and a thermal annealing step is often needed to obtain sufficiently crystallized materials [10].

In this paper, we report on recent progress of an original growth method that achieves very fast growth of ZnO nanostructures. Indeed, various ZnO nanostructures can be synthesized on fused quartz substrates within few seconds of irradiation of a droplet of methanolic zinc acetate dihydrate solution by an infrared continuous wave CO_2 laser. By using an infrared laser as the energy source (instead of a furnace or autoclave), our method is shown to offer the possibility of synthesizing the same types of ZnO nanostructures produced by the classical furnace-based methods but at a much faster rate, and most importantly, without the addition of an alkaline compound to induce favourable basic solution conditions. The method described here is a variation of laser-induced chemical liquid deposition (LCLD), which has been predominantly used for the deposition of metallic thin films and lines for microelectronics applications [14]. Only few papers report the use of LCLD for the synthesis of nanostructures and are generally limited to the growth of nanoparticles [15] and nano-islands [16] using excimer lasers.

The specific effect of laser parameters (i.e., laser power and irradiation time) on nanostructure morphology and microstructure was previously reported using a different chemical system, a solution of water and ethanol saturated by Zinc Acetylacetonate Hydrate ($Zn(AcAc)_2 \bullet H_2O$, ZAH) [17]. During this analysis, it was found that, logically, the absorbed laser energy plays a very important role in the formation of the deposits. For instance, a certain laser power threshold has to be reached to synthesize stoichiometric ZnO and another higher threshold to grow well formed ZnO nanostructures. These laser power thresholds depend on the irradiation time, on the nature and geometry of the absorption medium and on the

dissociation temperature of the precursor. To avoid repetition, focus is now oriented on the effect of varying the precursor concentration and adding water and monoethanolamine (MEA) to the solutions, in order to define a comprehensive process map. Samples with specific representative morphologies were selected while trying to keep the laser parameters constant throughout the analysis. The chemical system used is now zinc acetate dihydrate in an alcoholic solvent, which is usually used for the growth of ZnO nanostructures by wet chemistry techniques [18]. Changes in the chemical system, combined to refinements of the experimental method, enabled higher reproducibility and selectivity compared to previous experiments reported in [17].

2. Experimental

Zinc acetate dihydrate ($Zn(CH_3CO_2)_2 \bullet 2H_2O$, 98-100 % purity, Alfa Aesar, referred to as ZAD hereon) was manually mixed for 2 minutes with methanol (MeOH, absolute 99.8% purity, Alfa Aesar), de-ionized H_2O and Monoethanolamine (MEA, pure, L.V. Lomas). Next, the solutions were mixed for 30 minutes in an ultrasonic bath. A droplet of the solution was then transferred to a fused quartz substrate (1.15 mm thick, Ted Pella) using a micropipette (typical volume used was 3 µL). The maximum thickness and planar width of the solution drops has been measured using a microscope coupled to a CCD camera. The droplet's center was then irradiated by an unfocused CO_2 laser (coherent DEOS 100L, λ = 10.6 µm, waist = 1.9 mm) in open air at normal incidence to the substrate. The laser was operated in the Gaussian first Transverse Electromagnetic Mode (TEM_{00}). The irradiation times investigated ranged from 2 to 20 s and the laser power was varied from 30 to 40 W, providing light intensities between 239

W/cm^2 and 318 W/cm^2. During irradiation, fumes were produced in the irradiated zone. The fumes are probably gaseous reaction by-products and were sometimes accompanied by a flame (resulting from solvent combustion) and/or a visible light glow. Table 1 summarizes the experimental parameters used, observations during growth, and the main nanostructures synthesized. The molar concentration of water takes into account the hydration water of ZAD.

The samples were observed using a field-emission environmental scanning electron microscope (Quanta 200 FEG-ESEM, FEI Company). A field-effect transmission electron microscope (Jeol JEM-2100F FEG-TEM, 200 kV) with a Gatan Ultrascan 1000 TEM camera was used to obtain selective area electron diffraction patterns (SAED) and bright field TEM images. The TEM samples were prepared by gently rubbing the as-deposited samples on TEM grids covered by a Formwar film (400 mesh). The SEM and TEM image analyses were done using the ImagePro 5.1 AMS software (Mediacybernetics). X-ray diffraction (XRD) patterns of the whole samples were taken using a Philips X'PERT diffractometer equipped with a Cu Kα X-ray source (λ = 1.541 Å). The acceleration voltage was 45 kV with a 40 mA current. The detector was scanned from 30° to 70° (2θ) at a speed of 0.01°/s in the grazing angle mode. The grazing incident angle of the X-rays was set at 2°. Raman spectroscopy was performed using an InVia Raman spectroscope (Renishaw) with a 25 mW Ar+ laser (λ = 514.5 nm) focused by a 50X lens. The photoluminescence (PL) spectra of two samples deposited on high grade low impurity fused quartz (Corning 7980, SPI supplies) were acquired using a pulsed KrF excimer laser (wavelength = 248 nm, pulse duration = 15 ns) at an average intensity of 10 mW/mm^2 and a repetition rate of 50 Hz. The emitted light was directly collected (without the use of any lens) by an optical fiber

and transmitted to a photo-spectrometer (HR 4000, Ocean Optics) covering the 200 to 1100 nm spectral range. The peak fitting and curve smoothing for the XRD patterns, PL and Raman spectra were done using WIRE 2.0 software (Renishaw).

3. Results and discussion

3.1 General observations

When a solution drop is transferred on a substrate, it usually expands and thins. The extent of this behaviour depends on both the solution's composition, which affects its viscosity and its wetting behaviour on the substrate surface, and the volume of solution laid on the substrate. For example, a droplet of 3 µL containing only ZAD and MeOH (sample 1) will spread to a width of 3.96 mm and a thickness of 0.47 mm after 10 s while a droplet of 3 µL containing ZAD, H_2O and MEA (sample 8), will spread to a width of 5.33 mm and a thickness of 0.35 mm after 10 s.

The LCLD process involves various simultaneous and complex physical and chemical processes. The process starts with the absorption of photons by the solution and/or by the fused quartz substrate. The level of absorption depends on the wavelength of the exciting laser and on the temperature and nature of the absorbing medium. In our case, the solution is relatively transparent unless water is added [19,20,21]. Otherwise, the only absorption in the solution is from a small concentration of precursor hydration water. On the other hand, the fused quartz substrate strongly absorbs the CO_2 laser's light.

As the IR photons do not possess sufficient energy to dissociate the components of the solution, the laser energy is primarily transformed into thermal energy once absorbed. For this

reason, LCLD using a CO_2 laser is only possible with low thermal expansion substrates. The solution is thus directly heated by the laser and heated from below by the substrate. The laser has a Gaussian intensity distribution which causes the initial temperature distribution to be Gaussian [22]. These conditions are known to induce strong convective flows in the liquid layer (Marangoni convection) due to the laser-induced thermal gradient, the main mechanism of heat redistribution and reagent transport in the LCLD process, especially for large laser beams [23]. The chemical reaction system will thus be kinetically limited and the growth rate will strongly depend on laser power.

The surface of the liquid layer will be modified due to the convection currents. Usually a depression is created in the centre of the liquid droplet as the liquid is pushed away at high speeds [24]. Simultaneously, the solution is inhomogeneously evaporated, inducing concentration related convection currents. The solution is also progressively transformed into a colloid, as the precursor starts to react and nuclei of ZnO are formed. These nuclei will be deposited on the surface of the substrate by heterogeneous nucleation and form a thin seed layer of ZnO. The nanostructured film will continue grow by incorporation of nuclei brought by the convection currents. Consequently, for most experiments, radial nanostructure morphology changes are observed. These three temperature-related effects will also dynamically modify the absorption medium and create a feedback mechanism with the absorption of the laser light. Additionally, the evaporation of the solution, the dehydration and the decomposition of ZAD will create bubbles of gas in the solution and modify the composition of the reacting atmosphere. Finally, once the solution is completely evaporated (estimated to occur in less than

2 s at 318 W/cm^2), the laser anneals the deposits, improving the crystalline quality, inducing grain growth and relaxing mechanical stresses in thin films [25].

3.2 Decomposition of ZAD in Methanol

Under non-basic conditions, three precursor clusters can form ZnO from ZAD: oxy-acetate or basic zinc acetate ($Zn_4O(Ac)_6$ and $Zn_{10}O_4(Ac)_{12}$), ethoxy-acetate ($(EtOZnAc)_n$) and hydroxy-acetate ($Zn_5(OH)_8(Ac)_2(H_2O)_2$) [18,26]. When heated slowly in air, ZAD is dehydrated from 80 to 115°C, melts around 250°C, and forms $Zn_4O(Ac)_6$ around 257°C [27]. When anhydrous ZA is heated in a low partial pressure of water vapour, it decomposes and forms ZnO after sublimation between 180 and 200 °C [28]. Maruyama *et al*. report an activation energy of 20.6 kJ/mol for the gas-phase deposition of ZnO films using an anhydrous ZA precursor [29]. Since the ZAD is subjected to very fast heating in the presence of water in our experiments, it is likely that the activation energy will be lower and that the following reaction mechanism applies:

$$Zn(CH_3CO_2)_2 \bullet 2H_2O \rightarrow Zn(CH_3CO_2)_2 + 2\ H_2O \quad (1)$$

$$Zn(CH_3CO_2)_2 + H_2O \rightarrow ZnO + 2\ CH_3COOH \quad (2)$$

Figure 1A shows a low magnification SEM image of the middle of a sample grown at a laser power of 40 W for 3 s with a solution containing only ZA and methanol (sample 1). Letters B, C and D refer to locations where the corresponding images of figure 1 were taken. In the vicinity of the centre of the deposit (X), a very thin film of small ZnO islands has grown but no notable nanostructures are visible. The sparse growth of elongated rod-like structures can be observed at the beginning of the “growth ring” (figure 1B). These “proto-rods” are less than 200

nm long, have an average diameter of 72 nm and an irregular shape. Rod growth becomes denser and the rods grow longer and thinner as we move farther from the centre. The densest growth area (50 rods μm^{-2}) is on the bright ring visible in figure 1A (figure 1C). The nanorods grow on small nodules in a generally upwards direction and a few grow laterally (average length = 341, average diameter = 30 nm, aspect ratio ≥ 10). Farther away from the sample centre, the nodules grow larger but fewer rods are found until they disappear completely, leaving the substrate covered by a porous ZnO film (figure 1D). The use of ZAD as a precursor produces deposits with significantly higher homogeneity than our earlier works with $Zn(AcAc)_2$ [17], where the nanostructures erratically grew on thick mounds of ZnO.

3.3 Effect of additives

The addition of the complexing and stabilizing agent MEA to a ZAD solution was shown to increase crystalline alignment along the *c* axis of wurtzite ZnO [30] and the yield of ZnO due to a higher pH [31]. On figures 2A (sample 1) and 2B (sample 2), two images taken at approximately the same distance from the centre of the sample (on the bright ring, region C in Fig. 1) can be compared. On figure 2A, the rods grow in a seemingly random direction. On figure 2B, the rods grown with added MEA are seen to be more vertically aligned and show hexagonal cross-sections. With MEA, the nanorods are also slightly larger (average diameter of 50 nm) and the growth is denser (62 rods μm^{-2}).

Lee *et al.* reported that increasing the relative humidity strongly influenced the alignment, density and nanorod size of ZnO nanorod arrays grown using ZAD/EtOH solutions [10]. The addition of H_2O to our precursor solution had a radical effect on the morphology of

the resulting ZnO nanostructures. On the sample synthesized at 30 W for 20 s (sample 3), near the centre of the laser beam (starting at ~200 μm), long tapered nanorods (nanoneedles) finishing in a sharp tip have grown on nodules (max length ~ 6 μm). A few μm away, the growth becomes denser but the nanoneedles are shorter (average length = 900 nm, average diameter = 46 nm, figure 2C). Roughly 400 μm from the centre, the nanostructure's morphology has evolved (inset of figure 2C). The nodules are bigger (some around 500 nm wide) and appear to be formed by aggregated faceted crystals. The nanoneedles are still present but much more hexagonal nanorods can be found. About 500 μm from the centre, nanorods with a hexagonal cross-section dominate. The rods and needles are shorter but the "seed" nodules have grown and cover most of the substrate. The nanostructures grow at the apex of the crystals forming the nodules, which gives them a random orientation with respect to the substrate.

This variation of morphology can be explained by a concentration gradient created by laser-induced convection in the solution droplet. Where the precursor concentration was low, only small isolated seed nodules grew and the rods grew in length instead of diameter, having fewer nucleation sites to initiate growth. As the building block access diminished with length, the diameter decreased, forming sharp tips. Where the precursor concentration was high, more ZnO crystals grew directly on the substrate, forming bigger nodules and allowing more rod-like structures to grow at the expense of their length.

A different kind of deposit is obtained when a droplet of 2 μL of the same solution is irradiated at 40 W for 5 s. The centre of sample 4 is covered by a dense growth of long (~ 4 μm) hexagonal nanorods (figure 2D). These nanorods are much wider than the other samples

(average diameter of 530 nm, see figure 2D, right inset) and generally grow in a direction perpendicular to the substrate's surface. This central growth region (about 400 μm wide) is surrounded by a wider field of short and tapered nanorods (~ 500 nm long) with almost circular cross-sections (figure 2D, left inset). Three or four nanorods can sprout from the same seed, growing in seemingly random directions. We can conclude here that the addition of water to the reaction system has increased the length and improved the alignment of the nanorods deposited in the centre of the laser beam while increasing the total volume of ZnO growth. These two samples also allow the comparison of results obtained at low intensity and long irradiation time (sample 3) and medium intensity and irradiation time (sample 4). From figures 2C and 2D, it can be seen that a lower laser power but longer irradiation time promotes the growth of longer and thinner nanorods at the expense of growth density. This is probably due to the five fold increase of laser annealing time (approximately 18 s vs 3 s).

3.4 Effect of precursor concentration

Figure 3A shows nanorods grown at 40 W for 3 s using a solution of 0.1 M/L of ZAD and equal concentration of MEA (sample 5). The rods of figure 3A have an average length of 521 nm and are very thin (diameter between 20 and 40 nm). Figure 3B shows sample 6, grown in the same conditions but at ZAD and MEA concentrations of 0.75 M/L. On the main image of figure 3B, growth is seen to be much denser than at 0.1 M/L, with the substrate almost completely covered by thin nanorods (average diameter ~ 53 nm) and larger nanorods (average diameter ~ 156 nm). Both kinds of rods have similar lengths (average length ~380 nm). The bottom inset of figure 3B shows a higher magnification view of a region of the sample where the larger rods

(average diameter ~ 224 nm) have grown without the smaller ones. The rods have a hexagonal cross-section, a ribbed texture and their tip is slightly tapered, terminating in a smaller flat hexagon.

The top inset of figure 3B shows a region of the sample 6 (centre of laser beam) where longer nanorods (~ 2 µm) with circular cross-section and ribbed texture have grown on small nodules. Figures 4A and B show higher magnification TEM images of this type of rods. The nanorod of figure 4A has a diameter of 166 nm and a wedge shaped tip. The SAED pattern of the nanorods (inset) shows that the nanorods are single crystalline. Three interplanar distances (*d*) were measured on the diffraction pattern (d_1 = 5.18 Å, d_2 = 2.82 Å and d_3 = 2.46 Å) and can be indexed using known values for wurtzite ZnO [32]. The occurrence of the normally forbidden 001 reflection is due to double diffraction. *From this, it can be deduced that the nanorods have grown in the [001] or* c *axis direction. This is confirmed in figure 4B, where crystallographic planes with an interplanar distance of 5.3* Å (close to the reference *c* axis value of 5.2 Å) are stacked in the growth direction. The ribbed texture of the nanorods walls may be caused by the adsorption of MEA on the crystal faces of the growing rods, forming Zn-MEA complexes inhibiting lateral crystal growth. Such growth behaviour has been previously observed with other surfactants like EDA and CTAB [13].

To test the combined effect of H_2O and MEA, H_2O was added to the solutions of samples 5 and 6, keeping the other concentrations constant. The solutions with added water remained white after ultrasonication, probably indicating that hydrolysis started right away and that a precursor cluster or ZnO was produced in solution. The addition of such a large quantity of

laser-absorbing H_2O in the solution presumably changed the way the droplets were heated during irradiation. For sample 7, almost no material is deposited in a radius of 1.25 mm around the beam centre. Short nanorods (~ 250 nm long) then start to grow on a nodular seed layer (inset of figure 3C). As the distance from the centre increases, the rods' diameter increases until they begin to fuse and form a porous film. Further out, at the edge of the laser beam (~ 2 mm from the centre), the short nanorods reappear but the growth is much denser (30 nanorods μm^{-2}, figure 3C). Such growth is observed on a ring approximately 0.75 mm wide. The nanorods have a hexagonal cross-section and an average diameter of 156 nm. Again, such radial morphology changes can be explained by laser-induced thermo-capillary convection. With a higher H_2O content, the surface of the solution droplet is quickly heated, which enhances convection and pushes the liquid outside the laser beam.

Sample 8 (figure 3D) exhibits the same ring structure as the less concentrated sample 7 but the centre is covered by a roughly circular 1 mm wide nanowire growth region. The nanowires (average length 300 nm, diameter between 15 and 35 nm) grow on a thick seed layer at random orientations. Figure 4C shows a TEM image of the seed layer with a few nanowires still attached to it. This seed layer is found to consist of randomly packed ZnO nanocrystals having different sizes in the 50-200 nm range. These nanocrystals are seen to be attached to each others by their crystalline facets. The crystals are randomly oriented, as is shown by the ring-like SAED pattern (inset of figure 4C). The first 7 diffraction ring can be indexed using the reference *d* values with less than 1% of error. Figure 4D shows a high resolution TEM image of the attachment between a nanowire and the seed layer while the inset shows a lower

magnification view. The nanowires appear to grow on the apex of the seed layer crystals. The nanowires grow by homoepitaxy on the seed layer in the *c* axis direction. Indeed, the lattice fringes (inter-fringe distance of 5.2 Å, corresponding to the *c* axis) show that there are no crystal discontinuities between the seed layer and the nanowire. The main influence of increasing ZAD concentration seems to be on the seed layer thickness. No important seed layer is visible for 0.1 M/L. Small seed crystals islands or nodules are visible on the substrate for 0.5 M/L. The seed layer becomes a continuous faceted thin film 1-3 micrometer thick for 0.75 M/L without H_2O. With added H_2O, the seed layer becomes a thick weakly attached crust forming in or on the surface of the solution droplet.

3.5 Effect of droplet geometry

As previously mentioned, the growth of long hexagonal nanorods on sample 4 was achieved with a very small droplet volume (2 µL). The size, shape and volume of the precursor solution droplet have an important effect on the morphology of the deposited nanostructures. For this reason, care has been taken to use a standardized volume of solution (3 µL) for the other samples. To investigate the influence of solution volume, samples 9 and 10 have been produced with the same laser parameters and solution as sample 4 but with different volumes. With a solution volume of 2 µL, the droplet was well spread on the substrate and, upon irradiation, fumes came out of the irradiated zone, accompanied by the emission of white light. Figure 5A shows that the resulting nanorods are short (~ 210 nm) and thin (~ 50 nm). The inset of figure 5A shows that some rods have a tapered shape with a hexagonal cross-section. The nanostructures grow on a faceted seed layer covering most of the substrate. An increase in

solution volume to 6 µL with a well spread droplet led to the combustion of the methanol solvent. The appearance of a tall blue flame in the irradiated region was observed at various experimental parameters and seems to be related to the volume and the shape of the droplet. A widely spread droplet increases the probability of solvent ignition by increasing the evaporation of the solvent before irradiation (and thus the combustible vapor pressure). This would indicate a dependence of the process on droplet contact area. Unfortunately, when the droplet is transferred from the micropipette to the substrate, it does not always wet the substrate exactly the same way, even if the volume is kept constant. Indeed, the contact area is also dependent on the approach speed of the droplet. This aspect of the process could benefit from the use of a robotic fluid delivery system or a spin coater.

The samples deposited with the methanol flame are all very similar to figure 5B. The centermost region (top inset of figure 5B) is covered by sphere-shaped ZnO particles (balls) of varying size (average diameter of 500 nm). As the distance from the centre increases, small nanoparticle excrescences sprout from the balls and their size increases (average width of 950 nm, main image of figure 5B, ~1 mm from the centre); some balls being as wide as 1.4 µm. Most of the bigger balls seem to rest on smaller ones. Further out (~3 mm from the centre), the number of linked nanoparticles increases until they completely hide the balls (bottom inset of figure 5B). The particles have an average size of 76 nm. This film morphology covers most of the deposited area, a circle about 8 mm wide. We suggest that this change of morphology and growth mechanism when methanol combustion occurs is due to the increase of water content

and to a change of heating mode. Indeed, in addition to generating heat which will induce more nucleation, the combustion of methanol produces additional water vapor in the reaction zone:

$$2\ CH_3OH + 3\ O_2 \rightarrow 2\ CO_2 + 4\ H_2O \qquad (3)$$

H_2O could then hydrolyze the ZA to create ZnO by the intermediary of basic zinc acetate ($Zn_4O(Ac)_6$), a process which has been observed in spray pyrolysis experiments with ZAD [33].

X-ray diffraction patterns were obtained for samples 9 and 10 (Figure 6A). The goal was to observe the effect of methanol combustion on the material's crystallinity. Both samples exhibit the first 9 peaks of wurtzite ZnO with less than 2% shift from the reference 2ϑ, although the (102), (200) and (201) peaks of sample 9 are barely visible above the noise [32]. The average crystallite size was estimated from the (101) peak's width at half maximum intensity using Scherrer's formula and values of 22 and 60 nm were calculated for samples 9 and 10, respectively. This increase in crystallite size for sample 10 can be attributed to the flame-favored growth.

When comparing the peak's intensities relative to the most intense peak in the pattern ($R_{hkl} = \frac{I_{hkl}}{I_{101}}$) with the reference sheet's relative intensities (R_{hklref}) [32], an increase of relative intensity for the (100) and (110) peaks and a decrease for the other (*hkl*) peaks can be noticed for sample 9. The (100) and (110) relative intensities of sample 9 are higher by 47% and 40% with respect to the reference sheet, respectively (i.e. $\frac{R_{100} - R_{100ref}}{R_{100ref}} = 0.47$). For sample 10, the (100), (110) and (200) peaks are more intense by 29%, 7% and 23%, respectively. The higher relative intensity is probably an indication of a preferred crystalline orientation for both

samples. For sample 9, considering that the nanorods grow along the [001] direction (see figure 4), this would mean that the majority of the nanorods have grown parallel or at 45° to the substrate. More detailed XRD measurements (i.e. pole figure analysis) are required to conclude on this matter.

The PL spectra of the centre of samples 9 and 10 (see figure 5) are shown in figure 6B. Both spectra present only one feature in the UV region at 390 and 393 nm, respectively. The peak intensity of sample 10 is approximately 3 times higher than that of sample 9. It is well known that this UV emission peak is caused by the recombination of excitons and that the signal in the visible region (which is not even visible in our samples) is a signature of the presence of defects (such as oxygen vacancies) that cause deep level emission [34]. The red-shift of the UV peak (usually the near-band-edge emission is at 380 nm) is believed to be caused here by the laser annealing which modifies the band-gap of the ZnO crystals and increases the intensity of their PL emission [5]. Methanol combustion probably induces a higher temperature and thus a higher red-shift and intensity for sample 10. The difference in intensity can also be caused by nanostructure morphology differences. The increased surface area of the nanoballs and nanoparticles of sample 10 might contribute to the observed increase of its PL emission intensity [35].

Figure 7 shows Raman spectra taken in various regions of sample 11. Spectrum 1 was acquired in the central region of sample 11, where ZnO balls were visible at the optical microscope. Spectrum 2 was acquired further away from the centre of sample 11, where nanoparticles such as those seen in the bottom inset of figure 5B have grown. Finally, spectrum

3 was acquired in the outer region of sample 11 (~ 7 mm from the centre), where a sort of thick crystallized film could be found. On spectrum 1, two peaks associated with bulk ZnO are present: the A_1 TO (Transverse Optical) peak at 382 cm^{-1} and the E_2 High at 437 cm^{-1} [36]. On spectrum 2, the same peaks are found at 383 and 437 cm^{-1} respectively with the addition of the E_1 TO peak at 413 cm^{-1}. For both spectra, the E_2 H peak is very strong and narrow, indicating good crystalline order. The E_1 LO peak, normally associated with presence of oxygen vacancies along the *c* axis, is absent or too weak to be detected, as is the A_1 LO peak []. Peaks originating from the fused quartz substrate are present in both spectra: a broad feature around 440 cm^{-1} (ω_1) and peaks at 492 cm^{-1} (D_1), 605 cm^{-1} (D_2), 794 cm^{-1} (ω_3) and 1064 cm^{-1} (ω_4 TO) [37]. The other significant features of spectrum 1 (A_1 acoustic overtone at 330 cm^{-1} and others at 1166, 1674, 2330 cm^{-1}) are the result of combinations and overtones of ZnO and fused quartz. Growth is less dense in the centre of the sample, which results in more intense fused quartz peaks for spectrum 1. As was the case with the PL spectrum, the dense growth of nanoparticles (spectrum 2) scatters the exciting laser very well, resulting in an intense and well-defined wurtzite ZnO Raman spectrum.

Spectrum 3 is very different from spectrum 1 and 2, and shows the trademark vibration modes of the acetate ligand: the in-plane OCO rocking at 493 cm^{-1}, the out of plane OCO rocking at 613 cm^{-1}, the OCO symmetric bend at 675 cm^{-1}, the C-C symmetric stretch at 933 cm^{-1}, the out of plane CH_3 rocking at 1052 cm^{-1}, the CH_3 symmetric bend at 1344 cm^{-1}, the CO symmetric stretch at 1426 cm^{-1}, the CO asymmetric stretch at 1579 cm^{-1}, the CH_3 symmetric stretch at 2936 cm^{-1}, and the CH_3 asymmetric stretch at 2986 cm^{-1} [38]. The positions of these peaks are

all shifted by 10 to 15 cm^{-1} from the positions reported for ZAD [39,40]. Other differences from ZAD are the multiple peaks in the Zn-O vibration region: normally only one peak is present at 275 cm^{-1} while we have peaks at 150, 234, 287 and 398 cm^{-1}. The bands between 3000 and 3600 cm^{-1} are normally associated to the OH vibrations of water but the last peak (the "free" OH peak) is more intense than usual [41]. These irregularities may indicate that we are not in the presence of ZAD but of one of the precursor clusters, either water with basic zinc acetate or hydroxy-acetate or a mix of the two.

4. Conclusion

By using the same chemical solutions as those usually used in the classical chemical route for the synthesis of ZnO, we demonstrate the successful growth of various types of ZnO nanostructures (and thin films) using an infrared laser as an energy source, and this, on a markedly shorter time scale than in classical methods. The results obtained in the present work were found to overcome some of the issues encountered in our previous work [17] and offer more latitude to control the growth of ZnO nanostructures. Of particular interest is the radial variation in nanostructure morphology obtained here, in contrast with the seemingly random variation previously observed with the $Zn(AcAc)_2$ precursor. This is thought to be caused by laser-induced concentration and surface tension gradients. Also, the use of ZAD instead of $Zn(AcAc)_2$ and of droplets of lower volume allowed the growth of much more homogeneous deposits directly on the substrate. The ZnO nanorods grow along the *c* axis of wurtzite ZnO, on the apex of randomly oriented ZnO nanocrystals forming an underlying seed layer. The addition of MEA and H_2O to the solutions enhanced rod growth and alignment. An increase in ZAD

concentration increased the thickness of the seed layer. Raman and PL spectroscopy results suggest that the synthesized ZnO nanostructures are of high crystalline quality with very low level of defects. These results will lead to the establishment of a partial process map since they allowed identification of the appropriate laser and solution parameters to grow specific types of nanostructures. It was also found that the shape and size of the solution droplet had a non negligible influence on the resulting ZnO nanostructures. Conditions that favour methanol ignition can drastically affect the morphology of the deposits. To obtain higher reproducibility and selectivity, further research has to be done on ways to reduce the influence of laser-induced convection in the solution droplet, on a reproducible solution transfer method and on the determination of the effects of droplet volume on deposit morphology. Addressing these current limitations may lead to a fast and cheap process capable of locally depositing photoluminescent ZnO nanostructures.

Acknowledgments

The authors gratefully acknowledge funding for this project by the Natural Sciences and Engineering Research Council of Canada and the Canadian Foundation for Innovation. Financial support for Dr. Christian Fauteux was provided by the government of Québec (Fonds Québécois de la Recherche sur la Nature et les Technologies). The authors also thank Jean-Philippe Masse, Dr. Rémi Longtin, Amine El Mourid and Dr. Riadh Smirani for assistance with characterization and valuable comments.

References

1. G. C. Yi, C. Wang, W. I. Park, Semicond. Sci. Technol. 20 (2005) S22
2. Z. L. Wang, Mater. Today 7:6 (2004) 26
3. J. J. Wu, S. C. Liu, Adv. Mat. 14 (2002) 215
4. X. Y. Kong, Y. Ding, Z. L. Wang, J. Phys. Chem. B 108 (2004) 570
5. S. Cho, J. Ma, Y. Kim, Y. Sun, G. K. L. Wong, J. B. Ketterson, Appl. Phys. Lett. 75 (1999) 2761
6. X. Q. Wei, B. Y. Man, M. Liu, C. S. Xue, H. Z. Zhyang, C. Yang, Physica 388 (2007) 145
7. Y. Li, G. W. Meng, L. D. Zhang, Appl. Phys. Lett. 76 (2000) 2011
8. T. Ma, M. Guo, Y. Zhang, X. Wang, Nanotechnology, 18 (2007) 035605
9. L. E. Greene, B. D. Yukas, M. Law, D. Zitoun, P. Yang, Inorg. Chem. 45 (2006) 7535
10. Y-J. Lee, T. L. Sounart, D. A. Scrymgeour, J. A. Voigt, J. W. P. Hsu, J. Cryst. Growth 304 (2007) 80
11. S. E. Ahn, J. S. Lee, H. Kim, S. Kim, B. H. Kang, K. H. Kim, G. T. Kim, Appl. Phys. Lett. 84 (2004) 5022
12. L. Vayssieres, N. Beermann, S.-E. Lindquist, A. Hagfeldt, Chem. Mater. 13 (2001) 233
13. B. Liu, H. C. Zeng, Langmuir 20 (2004) 4196
14. K. Kordas, J. Bekesi, R. Vajtai, L. Nanai, S. Leppavuori, A. Uusimaki, K. Bali, Thomas F. George, G. Galbacs, F. Ignacz, P. Moilanen, Appl. Surf. Sci. 172 (2001) 178
15. Z. C. Zhong, R. H. Cheng, J. Bosley, P. A. Dowben, D. J. Sellmyer, Appl. Surf. Sci. 181 (2001) 196

16. Ouchi , Z. Bastl, J. Boháček, J. Šubrt, J. Pola, Surf. Coat. Technol. 201 (2007) 4728

17. C. Fauteux, R. Longtin, J. Pegna, D. Therriault, Inorg. Chem. 46 (2007) 11036

18. L. Spanhel, J. Sol-Gel Sci. Techn. 39 (2006) 7

19. R.A. Johnson, A.E. Stanley, Appl. Spectrosc. 42 (1988) 1268

20. T. Baba, A. Kobayashi, Y. Kawanami, K. Inazu, A. Ishikawa, T. Echizenn, K. Murai, S. Aso, M. Inomata, Green Chem. 7 (2005) 159

21. M.L. Wolbarsht, IEEE J. Quant. Electron. 20 (1984) 1427

22. M. Lax, J. Appl. Phys., 48 (1977) 3919

23. M. R. Brook, K. I. Grandberg, G. A. Shafeev, Appl. Phys. A 52 (1991) 78

24. G. G. Gladush, L. S. Krasitskaya, E. B. Levchenko, A. L. Chernyakov, Sov. J. Quantum Electron. 12 (1982) 408

25. R. Hong, C. Wei, H. He, Z. Fan, J. Shao, Thin Solid Films 485 (2005) 262

26. E. Hosono, S. Fujihara, T. Kimura, H. Imai, J. Sol-Gel Sci. Technol. 29 (2004) 71

27. L. Hiltunen, M. Leskelä, M. Mäkelä, L. Niinistö, Acta Chem. Scand. A 41 (1987) 548

28. T. Arii, A. Kishi, Thermochim. Acta 400 (2003) 175

29. T. Maruyama, J. Shionoya, J. Mater. Sci. Lett. 11 (192) 170

30. M. Ohyama, H. Kozuka, T. Yoko, Thin solid films 306 (1997) 78

31. L. Znaidi, G.J.A.A. Soler Illia, S. Benyahia, C. Sanchez, A.V. Kanaev, Thin solid films 428 (2003) 257

32. JCPDS card 36–1451, ZnO

33. F. Paraguay D., W. Estrada L., D.R. Acosta N, E. Andrade, M. Miki-Yoshida, Thin Solid Films 350 (1999) 192

34. J. Lim, K. Shin, H. W. Kim, C. Lee, J. Lumin. 109 (2004) 181

35. W. S. Shi, B. Cheng, L. Zhang, E.T. Samulski, J. Appl. Phys. 98 (2005) 083502

36. T.C. Damen, S. P. S. Porto, B. Tell, Phys. Rev. 142 (1966) 570

37. A. E. Geissberger, F. L. Galeener, Phys. Rev. B 28 (1983) 3266

38. V. Koleva, D. Stoilova, J. Mol. Struct. 611 (2002) 1

39. M. M. Yang, D. A. Crerar, D. E. Irish, Geochim. Cosmochim. Acta 53 (1989) 319

40. R. D. Yang, S. Tripathy, Y. Li, H.-J. S., Chem. Phys. Lett. 411 (2005) 150

41. V. Crupi, F. Longo, D. Majolino, V. Venuti, Eur. Phys. J. Special Topics 141 (2007) 6164

Figure captions

Figure 1: A) Low mag. SEM image of the deposit (sample 1). X indicates the centre of the laser beam, B) Proto-rods found 1 mm from the centre, C) Nanorods found 1.5 mm from the centre, D) Nanorods found outside the main deposition ring.

Figure 2: Effect of MEA and water: A) Nanorods grown without MEA (sample 1), B) Nanorods grown with MEA (sample 2), C) Nanoneedles grown with H2O (sample 3), D) Nanorods grown with H2O (sample 4).

Figure 3: Effect of ZAD concentration A) Low concentration with MEA (Sample 5), B) High concentration with MEA (Sample 6), C) Low concentration with H2O and MEA (Sample 7), D) High concentration with H2O and MEA (Sample 8).

Figure 4: TEM images and SAED patterns of A) Nanorods grown at high ZAD concentration with MEA (sample 6), B) High magnification view of A (Sample 6), C) Seed layer and nanowires at high ZAD and water concentration with MEA (sample 8), D) Attachment of nanowires on seed layer (sample 8).

Figure 5: Effect of MeOH combustion: A) Sparse nanorod growth without combustion (2 µL of solution, sample 9), B) Nanoballs and nanoparticles with combustion (6 µL of solution, sample 10)

Figure 6: A) XRD pattern of sample 9 (without combustion, sparse nanorod growth) and 10 (with combustion, nanoballs and nanoparticles), B) PL spectra of sample 9 and 10.

Figure 7: Raman spectrum of sample 11: (1) centre of growth region (Nanoballs) (2) exterior of growth region (nanoparticles) (3) outside of growth region

Tables

Table 1: experimental parameters

#	ZAD (M/L)	H_2O (M/L)	MEA (M/L)	Intensity (W/cm^2)	Irr. Time (s)	Observations	Main results
1	0.5	0.082	0	318	3		Thin and short nanorods
2	0.5	0.082	1.6	318	3	Fumes, white glow	Tapered and hexagonal nanorods
3	0.5	2.86	0	239	20	Fumes, white glow	Long nanoneedles
4				318	5		Long hexagonal nanorods
5	0.1	0.016	0.1	318	3		Thin nanorods with tapered tips
6	0.75	0.123	0.75	318	3	Fumes, orange glow	Ribbed nanorods with tapered tips and nanowires
7	0.1	10.01	0.1	318	5	Fumes, orange glow	Very short hexagonal nanorods
8	0.75	10.11	0.75	318	3	Fumes	Nanowires and nanonails
9	0.5	2.86	0	318	5	Fumes, white glow	Short nanorods
10						Large flame, fumes, white glow	Nanoballs and nanoparticles
11	0.5	0.082	0	318	3	Flame	Nanoballs and nanoparticles

Figures

Figure 1

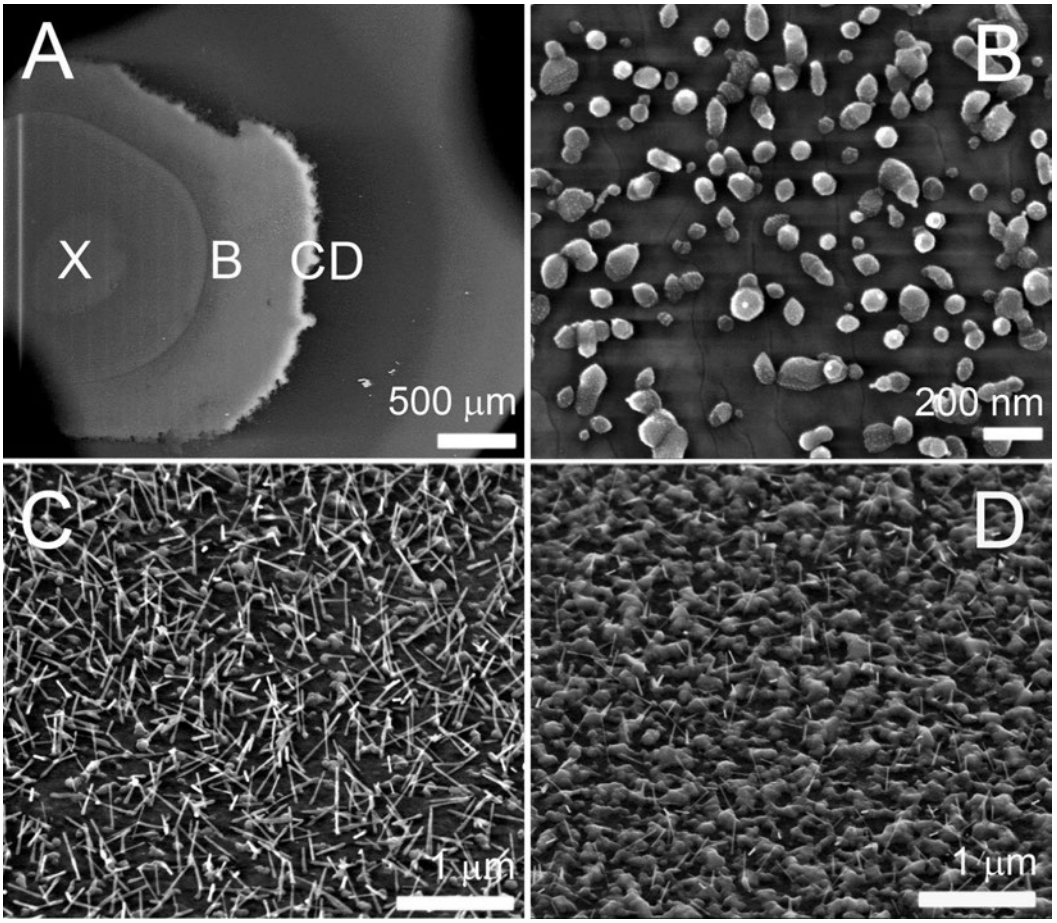

Figure 2

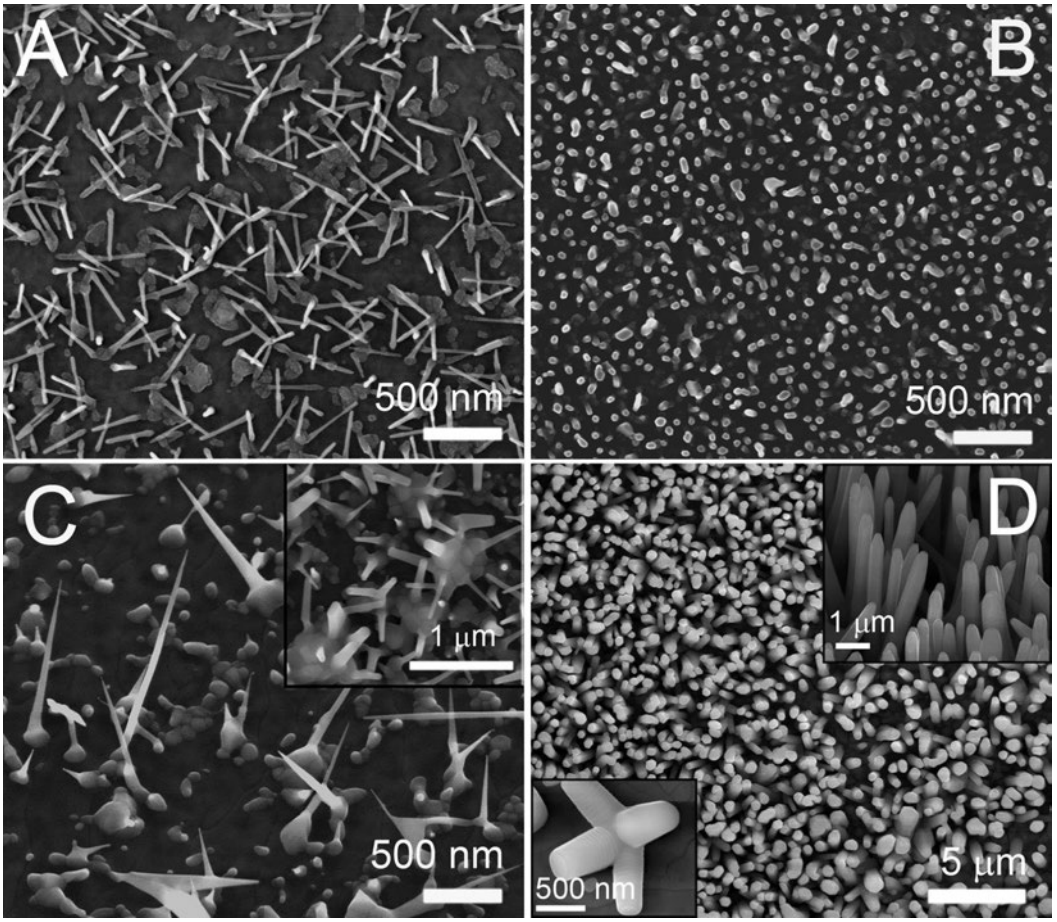

Figure 3

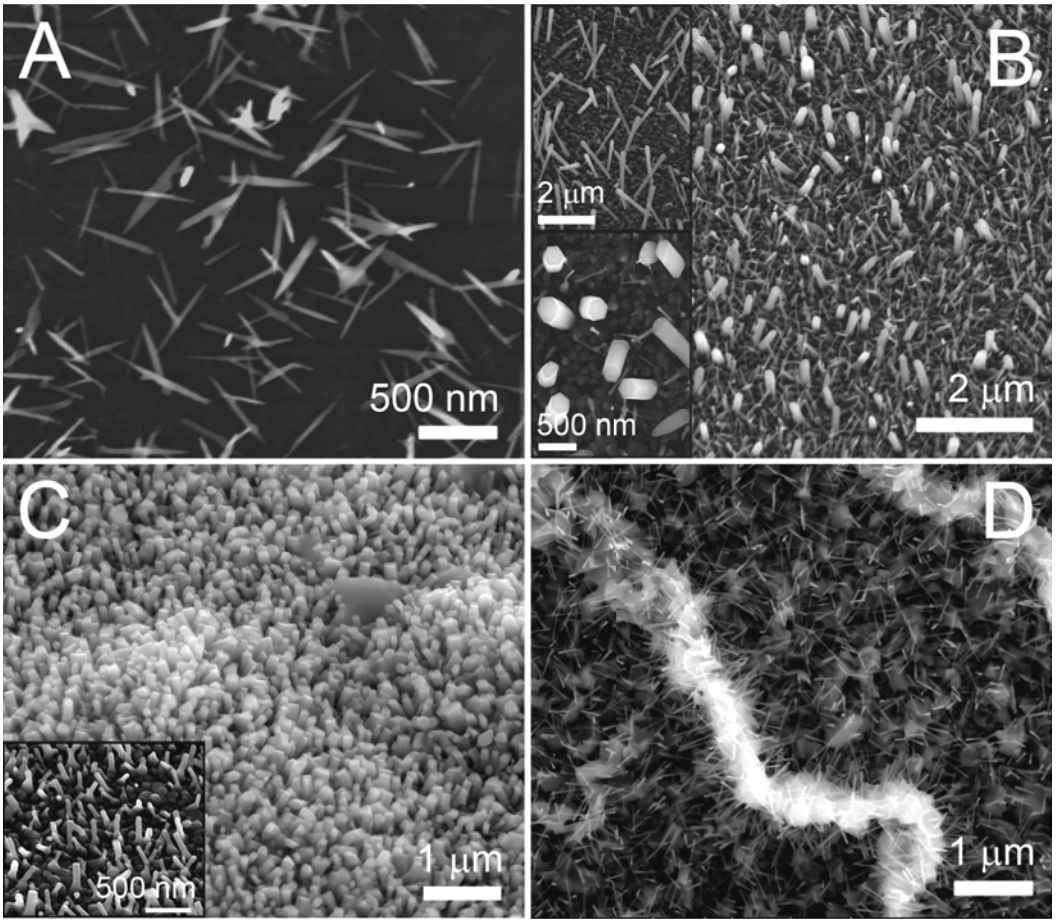

Figure 4

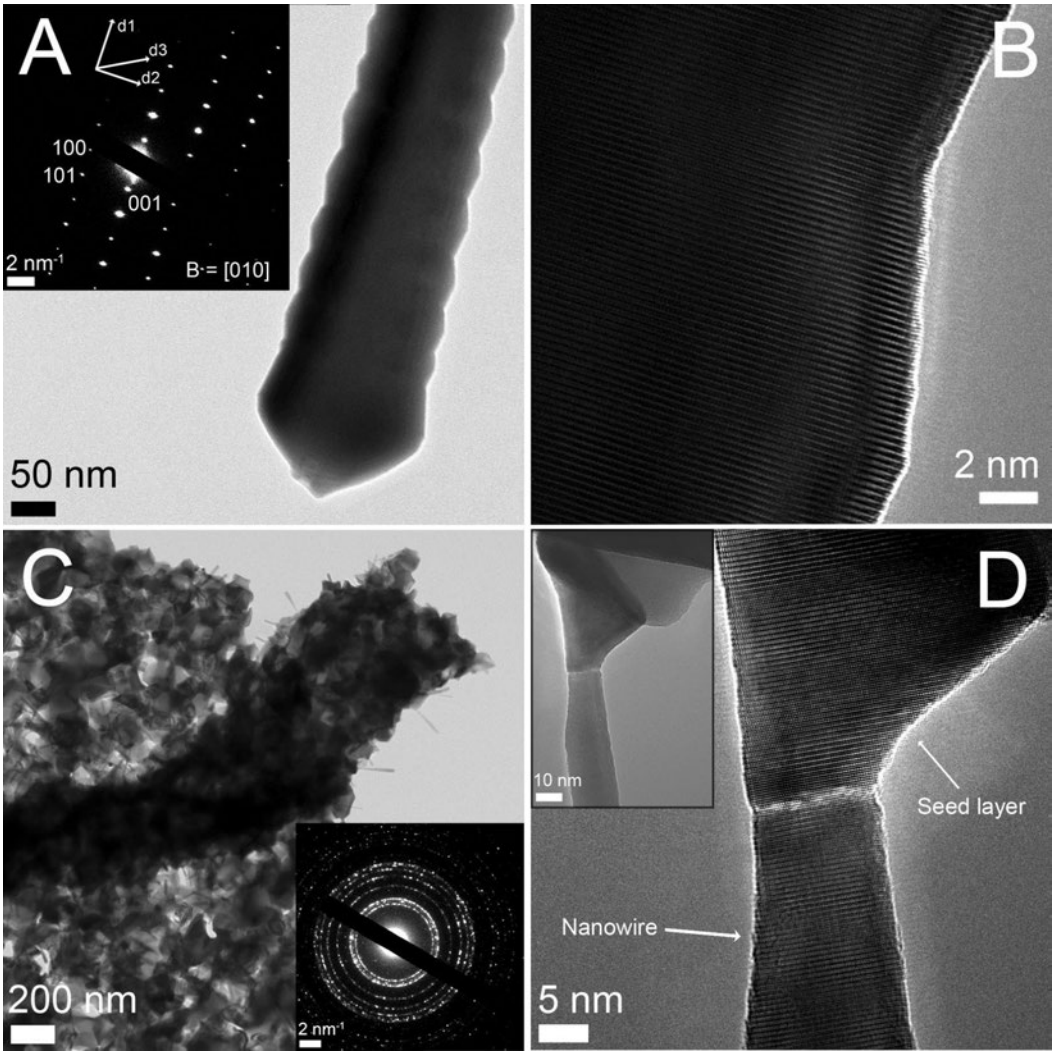
A
d1
d3
d2
100
101
001
2 nm-1
B = [010]
50 nm
B
2 nm
C
200 nm
2 nm-1
D
10 nm
Seed layer
Nanowire
5 nm

Figure 5

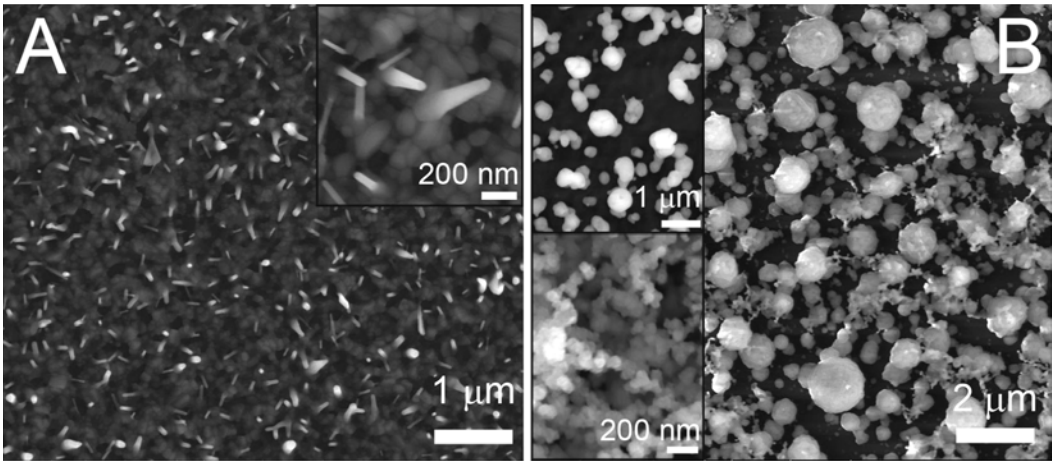

Figure 6

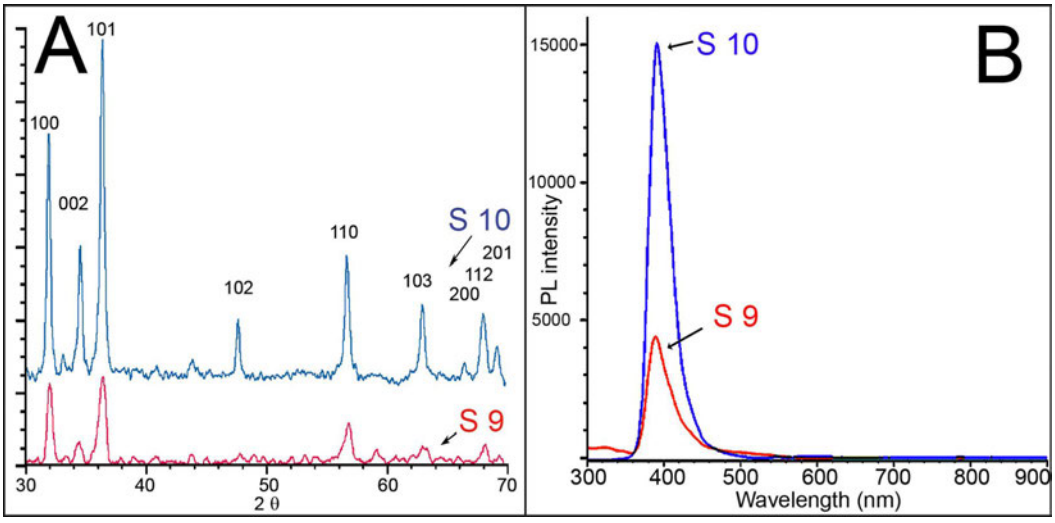
A
101
100
002
102
110
103
200
112
201
S 10
S 9
30
40
50
60
70
2 θ
B
S 10
S 9
15000
10000
5000
PL intensity
300
400
500
600
700
800
900
Wavelength (nm)

Figure 7

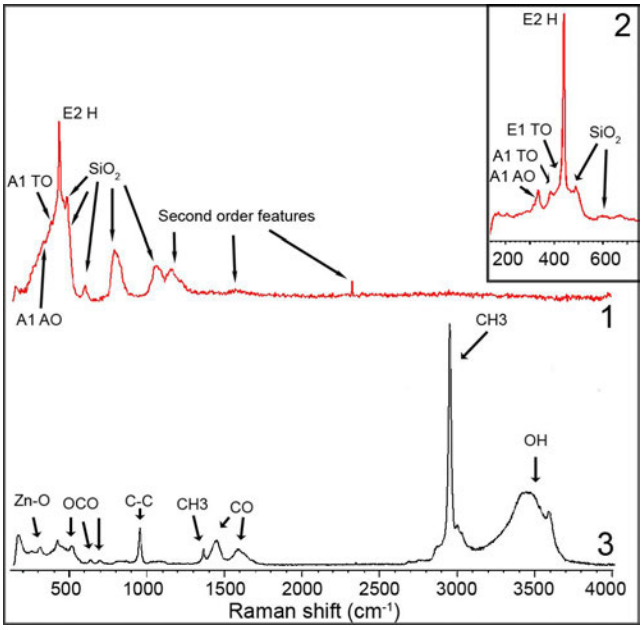
E2 H
2
E1 TO
A1 TO
A1 AO
SiO2
200 400 600
E2 H
A1 TO
SiO2
Second order features
A1 AO
1
CH3
OH
Zn-O
OCO
C-C
CH3
CO
3
500 1000 1500 2000 2500 3000 3500 4000
Raman shift (cm-1)